In-situ nanobeam X-ray diffraction of local strain in AlGaN/GaN MOS HEMT under transistor operation

Akihiro Shimada[1], Haruna Shiomi[1], Tetsuya Tohei[1,a)], Yusuke Hayashi[1,b)], Masaya Yamaguchi[1], Junpei Yamamoto[1], Takeaki Hamachi[1], Yasuhiko Imai[2], Kazushi Sumitani[2], Shigeru Kimura[2], Shota Kaneki[3], Tamotsu Hashizume[3,c)], and Akira Sakai[1,a)]

[1]Graduate School of Engineering Science, The University of Osaka, 1-3 Machikaneyama-Cho, Toyonaka, Osaka 560-8531, Japan

[2]Japan Synchrotron Radiation Research Institute, Sayo, Hyogo 679-5198, Japan

[3]Research Center for Integrated Quantum Electronics, Hokkaido University, Sapporo 060-8628, Japan

[a)]**Authors to whom correspondence should be addressed:** tohei@ee.es.osaka-u.ac.jp and sakai@ee.es.osaka-u.ac.jp

[b)]**Present address:** National Institute for Materials Science, 1-2-1 Sengen, Tsukuba, Ibaraki 305-0047, Japan

[c)]**Present address:** Institute of Materials and Systems for Sustainability, Nagoya University, Furo-cho, Chikusa-ku, Nagoya 464-8601, Japan

In-situ nanobeam X-ray diffraction of local strain in AlGaN/GaN MOS HEMT under transistor operation

Abstract

We combined synchrotron radiation nanobeam X-ray diffraction technique with the pump-probe method to perform in-situ measurements of local strain in a normally-ON AlGaN/GaN metal-oxide-semiconductor high electron mobility transistor device under transistor operation. The *c*-axis strain in the AlGaN barrier layer within the gate region exhibited a clear position dependence, increasing as the gate voltage was increased in the negative direction and as the measurement position moved from the center of the gate electrode towards the drain-side gate edge. Based on the characteristics of the measured *c*-axis and *a*-axis strains, we successfully extracted not only the strain component due to the inverse piezoelectric effect but also the thermal expansion strain component, using the constitutive equation for elastic bodies. From the characteristics of the device current measured simultaneously with the strain measurements, it was revealed that the temperature rise inducing the thermal expansion strain was caused by the transient and steady-state drain currents.

I. INTRODUCTION

Power electronic devices based on Si are widely used in consumer electronics, electric vehicles, and power generation plants. However, further performance improvement to meet demands for high breakdown voltage and low on-resistance is reaching limitation in terms of the material properties. Gallium nitride (GaN) has attracted much attention as an alternative power device material because of its wider bandgap than Si and its high breakdown voltage.[1] Among those nitride-based devices, a high electron mobility transistor (HEMT) involving AlGaN/GaN heteroepitaxial structures has been developed and used practically in applications such as cellar phone base stations.[2] A broad range of power device applications are expected due to the merits of their low on-resistance and high-frequency operation, as well as their compact size and low power consumption.[3] In the AlGaN/GaN HEMT, a high concentration of carriers called two-dimensional electron gas (2DEG) is formed at the AlGaN/GaN interface by spontaneous polarization of the group III-nitrides and piezoelectric polarization caused by the lattice mismatch strain between AlGaN and GaN.[4] On the other hand, there are problems to be solved to further improve the performance and reliability of the devices. It has been reported that a local electric field concentration at the drain-side gate edge increases the stress due to the inverse piezoelectric effect and induces lattice defects such as pits, cracks, etc.,[5-15] which leads to degradation of device performance. Although various studies have been conducted to clarify the degradation mechanisms associated with defect formation in devices, few studies have focused on the lattice deformation dynamics in the local region caused by the inverse piezoelectric effect and other relevant factors under device operation.

An X-ray diffraction technique is one of the most effective methods to observe the deformation of crystal structure and the related strain.[16-20] Recently we have developed a pump-probe measurement method based on synchrotron radiation nanobeam X-ray diffraction (nanoXRD).[19] Utilization of pulsed synchrotron radiation at the facility SPring-8, enables non-destructive and in-situ observation of crystal structures in the device under operation. Our previous report evaluated the local lattice deformation of AlGaN/GaN metal-oxide-semiconductor (MOS) HEMTs, in which the inverse piezoelectric response of AlGaN *c*-plane spacing to the gate voltage application was clearly detected on a nanosecond time resolution.[19] In the previous study, however, only the gate voltage was applied to the device to verify the occurrence and detectability of the piezoelectric effect, so strain distribution under the transistor operation of the HEMT has been still elusive. In this study, we performed in-situ nanoXRD measurements of the local lattice strain in the AlGaN/GaN MOS-HEMT under transistor operation, i.e.,

simultaneous application of gate and drain voltages. Based on the systematic measurements and the analysis using the constitutive equation for elastic bodies, dominant factors inducing the strain in the device have been discussed. Results obtained in the present study provide useful information on the underlying physical mechanisms behind the device operation of GaN power devices with improved performance and reliability.

II. EXPERIMENTAL

The stacked structure of the AlGaN/GaN MOS-HEMT sample[21] evaluated in this study, is shown in Fig. 1(a). First, a highly resistive C-doped GaN layer (600 nm) was formed on the n-GaN substrate to prevent leakage current to the n-GaN substrate side. An undoped-GaN layer (900 nm) and the AlGaN barrier layer were formed to induce 2DEG at the interface. Considering the critical film thickness, the thickness and Al content of the AlGaN layer were set to be 20 nm and 20%, respectively. The density and the mobility of 2DEG were 6.5×10^{12} cm^{-2} and 1750 cm^2 V^{-1} s^{-1}, respectively. Ti/Al/Ti/Au as source/drain electrodes were formed on the AlGaN layer by electron beam deposition followed by annealing at 830 °C for 1 min to form an alloy. Al_2O_3 (30 nm) was then deposited by atomic layer deposition as a gate insulator film. The Ni/Au was deposited as a gate electrode using the same process as that for the source/drain electrodes. In this measurement, we adopted the long gate structure to investigate the position dependence and reproducibility in diffraction experiments and the gate length and width were 800 μm and 400 μm, respectively. We carried out post-metallization annealing (PMA) at 300 °C in N_2 after the MOS-HEMT fabrication to improve interface state density between the Al_2O_3/AlGaN. We confirmed that the PMA process reduced interface state densities at the Al_2O_3/GaN interface, down to 4×10^{10} cm^{-1} eV^{-1} at energies near the conduction band edge of GaN.[22] The electrical characteristics of the device showing well-defined normally-ON nature are described in detail in Ref 19.

The measurement geometry of nanoXRD (BL13XU beamline of SPring-8) is shown in Fig. 1(b). The synchrotron X-ray beam was focused at 430 nm × 1030 nm using a Fresnel zone plate and irradiated along the *m*-axis of the device under the drain and gate voltage application using a function generator. The X-ray probe size is smaller than the dimension of the gate and it allows the study of position dependence of lattice strain. The diffracted X-rays from AlGaN symmetric 0004 and asymmetric 1-104 were detected by two-dimensional photon-counting detector HyPix-3000 (Rigaku, Japan). In the present experimental condition X-rays can penetrate the gate metal and diffraction from AlGaN

layer and GaN layer are acquired. Since AlGaN and GaN shows different peak positions we can evaluate the strain of individual AlGaN layer. Three-dimensional (3D) ω–2θ–φ mapping was performed for the diffraction[16,19,20]; to quantify the 2θ value corresponding to the lattice spacing, the measured 3D diffraction profiles were integrated over the ω and φ directions to obtain one-dimensional 2θ profiles. Representative data of ω–2θ intensity map and 2θ-intensity profile are shown in Fig. S3. The lattice spacing was calculated from the peak in 2θ profiles and Bragg's equation. The strain resolution determined by the pixel size (100 ×100 μm^2) and the sample-detector distance (999.5652 mm) was 5.6×10^{-5}.

Next, we describe the pump-probe method used in this study. We applied the voltage as a pump pulse that was synchronized with the X-ray irradiation as a probe pulse and measured the local lattice deformation of the device under transistor operation. The used synchrotron X-rays have a period of 4.789 μs (frequency: 208.8 kHz) and consists of continuous X-ray pulses with a period of 1.815 μs, called "train section", and isolated X-ray pulses with a width of 60 ps, called "single bunch". Synchronizing these X-ray pulses with the applied voltage and changing the phase of the applied voltage pulses enables to irradiate the probe X-ray pulses at any desired timing. In this study, only the train section was selectively irradiated to the operating device. Schematic circuit diagram of the experimental setup for the electrical measurement system are shown in Fig. S4.

III. RESULTS AND DISCUSSION

We applied a pulse voltage of -7, -5, -3, and 0 V as the gate voltage V_g and a pulse voltage of 0 and 5 V as the drain voltage V_d and observed AlGaN 1-104 diffraction spots to measure the voltage dependence of strains along the *c*- and *a*-axis. Although the AlGaN layer of the sample used in this study has compressive strain along the *c*-axis in its non-operating state, the strain is defined based on the lattice spacing in the absence of an applied voltage, specifically the initial spacings of the *c*- and *a*-planes that exhibit compressive and biaxial tensile strains, respectively. The local strain was evaluated at four measurement points of nanoXRD: 400, 200, 50, and 10 μm apart from the drain-side gate edge (named as points A, B, C, and D, respectively). Results of the *c*- and *a*-axis strains of the AlGaN layer measured at points A to D as a function of V_g with different V_d are summarized in Fig. 2. We observed that the *c*-axis strain increases linearly with increasing V_g in the negative direction. This indicates the applied external electric field reduces the polarization of the AlGaN layer, and the pre-existing *c*-axis compressive strain decreases accordingly with increasing the electric field.[19] It is also notable that the strain tended to be higher when V_d was set to 5 V (blue plots) compared to 0 V (red plots)

and higher strain was detected at the measurement points closer to the drain-side gate edge. Meanwhile, the *a*-axis strain was below the detection limit, which is contrary to the expectation of compressive strain due to the inverse piezoelectric effect. We assume that this situation is due to the compressive strain being offset by the thermal expansion strain caused by temperature rise, implying that the *c*-axis strain increases not only due to the inverse piezoelectric effect but also due to thermal expansion strain. This assumption is highly plausible because it has been frequently reported that when drain current flows in HEMT devices, the temperature rise occurs from the gate to the drain regions in the device due to the Joule heating effect.[23-28]

Based on this assumption, we attempt to estimate the temperature rise in the device using the constitutive equation for elastic bodies. Given that the strain of the AlGaN layer consists of three components such as constrained strain due to the substrate underneath the AlGaN layer, inverse piezoelectric strain due to the voltage application, and thermal expansion strain, the measured strains can be expressed by the following equation.

$$\begin{pmatrix}\varepsilon_{xx}\\ \varepsilon_{yy}\\ \varepsilon_{zz}\\ \varepsilon_{yz}\\ \varepsilon_{zx}\\ \varepsilon_{xy}\end{pmatrix}=\begin{pmatrix}s_{11} & s_{12} & s_{13} & 0 & 0 & 0\\ s_{12} & s_{11} & s_{13} & 0 & 0 & 0\\ s_{13} & s_{13} & s_{33} & 0 & 0 & 0\\ 0 & 0 & 0 & s_{44} & 0 & 0\\ 0 & 0 & 0 & 0 & s_{44} & 0\\ 0 & 0 & 0 & 0 & 0 & s_{66}\end{pmatrix}\begin{pmatrix}\sigma_{xx}\\ \sigma_{yy}\\ \sigma_{zz}\\ \sigma_{yz}\\ \sigma_{zx}\\ \sigma_{xy}\end{pmatrix}+\begin{pmatrix}0 & 0 & d_{31}\\ 0 & 0 & d_{31}\\ 0 & 0 & d_{33}\\ 0 & d_{15} & 0\\ d_{15} & 0 & 0\\ 0 & 0 & 0\end{pmatrix}\begin{pmatrix}E_x\\ E_y\\ E_z\end{pmatrix}+\begin{pmatrix}\alpha_{11}\Delta T\\ \alpha_{11}\Delta T\\ \alpha_{33}\Delta T\\ 0\\ 0\\ 0\end{pmatrix} \quad (1)$$

where ε is the strain, E is the electric field strength, σ is the stress, d is the piezoelectric constant, α is the thermal expansion coefficient, and ΔT is the temperature rise. The z-axis is parallel to the *c*-axis. The effect of shear stress can be neglected and thus Eq. (1) can be simplified as

$$\begin{pmatrix}\varepsilon_{xx}\\ \varepsilon_{yy}\\ \varepsilon_{zz}\end{pmatrix}=\begin{pmatrix}s_{11} & s_{12} & s_{13}\\ s_{12} & s_{11} & s_{13}\\ s_{13} & s_{13} & s_{33}\end{pmatrix}\begin{pmatrix}\sigma_{xx}\\ \sigma_{yy}\\ \sigma_{zz}\end{pmatrix}+\begin{pmatrix}0 & 0 & d_{31}\\ 0 & 0 & d_{31}\\ 0 & 0 & d_{33}\end{pmatrix}\begin{pmatrix}E_x\\ E_y\\ E_z\end{pmatrix}+\begin{pmatrix}\alpha_{11}\Delta T\\ \alpha_{11}\Delta T\\ \alpha_{33}\Delta T\end{pmatrix}. \quad (2)$$

Considering the plane stress condition ($\sigma_{xx}=\sigma_{yy},\ \sigma_{zz}=0$), ε_{zz} is expressed from Eq. (2) as

$$\varepsilon_{zz}=\frac{2s_{13}}{s_{11}+s_{12}}\varepsilon_{xx}+\left(d_{33}-d_{31}\frac{2s_{13}}{s_{11}+s_{12}}\right)E_z+\left(\alpha_{33}-\alpha_{11}\frac{2s_{13}}{s_{11}+s_{12}}\right)\Delta T. \quad (3)$$

The coefficient of E_z in the second term on the right-hand side in Eq. (3), enclosed in the parentheses, is the piezoelectric constant d'_{33}, which accounts for the clamping effect of the substrate.[29,30] Therefore, ΔT is expressed as

$$\Delta T=\left(\varepsilon_{zz}-\frac{2s_{13}}{s_{11}+s_{12}}\varepsilon_{xx}-d'_{33}E_z\right)\Big/\left(\alpha_{33}-\alpha_{11}\frac{2s_{13}}{s_{11}+s_{12}}\right). \quad (4)$$

Here we consider each of variable in Eq. (4) in accordance with the experimental

conditions. First, we estimate E_z during device operation under the nanoXRD measurement. The electric field applied to the AlGaN layer was estimated using a finite element method (FEM) simulation (COMSOL Multiphysics). Details of the simulation are provided in the supporting information. In the simulation, we constructed a geometric model of the HEMT device (Fig. S1) and calculated E_Z exerted on the AlGaN layer under the applied gate and drain voltages. The simulation results of the electric field strength in the AlGaN layer at the moment of X-ray irradiation are shown in Fig. S2. The results indicate that in the absence of drain voltage, the electric field E_z remains nearly constant along the gate length, whereas with applied drain voltages, E_z varies from the drain-side edge of the gate electrode towards the center. Furthermore, the influence of the gate edge diminishes as the lateral geometry scale of the model increases. To estimate the piezoelectric strains at each measurement points, we adopted E_z values at the scaled positions corresponding to points A and D.

Second, the piezoelectric constant d'_{33} in Eq. (4) must be determined. Here we adopted d'_{33} value (2.18 pm/V), obtained from the previous experiment that accounted for the clamping effect.[19] For the thermal expansion coefficients and elastic compliances of $Al_{0.2}Ga_{0.8}N$, we used the following values obtained based on Vegard's law[31,32]: $\alpha_{11} = 3.77 \times 10^{-6}\ \mathrm{K}^{-1}$, $\alpha_{33} = 3.27 \times 10^{-6}\ \mathrm{K}^{-1}$, $S_{11} = 30.7 \times 10^{-4}$ GPa, $S_{12} = -9.70 \times 10^{-4}$ GPa, and $S_{13} = -5.68 \times 10^{-4}$ GPa.

Using these determined variables, the experimental *c*-axis strain values, ε_{zz} obtained at each measurement point, were analyzed using Eqs. (3) and Eq. (4) to derive individual strain components and temperature change ΔT, respectively. Figures 4(a-h) show results of individual strain components for points A and D respectively, from left to right: measured *c*-axis strain, constrained strain, inverse piezoelectric strain and thermal expansion strain as a function of V_g at different V_d. At point A, i.e., on the center of the gate electrode, the observed *c*-axis strain is approximately dominated by the contribution of the inverse piezoelectric strain, since their values are similar to each other. On the other hand, at point D, i.e. on the drain side of the gate electrode, the effect of not only the inverse piezoelectric strain but also the thermal expansion strain is found to be strong, particularly noticeable at a drain voltage of 5 V.

To elucidate the origin of the heat responsible for the thermal expansion strain, we analyzed the correlation between ΔT and device characteristics, particularly focusing on the drain current I_d during transistor operation. During the in-situ nanoXRD measurements, the time dependences of the applied V_d and V_g, as well as the I_d flowing through the device, were measured. The results at point A are presented as a representative example in Fig. 4(a). It is noteworthy that, in the time profile of I_d, a significant transient

drain current is observed at the rising edge of the applied pulse voltage, irrespective of V_d or V_g. Furthermore, this transient current coincides with the period during which the X-ray irradiation for diffraction is conducted. Here, we define the average current flowing through the device during X-ray irradiation as I_d'. The value of I_d' was evaluated by the integration of the transient current part in the measured I_d curve (red-filled area in Fig. 4(a)) divided by the time during which X-rays are irradiated. Figure 4(b) presents the calculated results of I_d' under various voltage application conditions at point A. Even when V_d is 0 V, I_d' increases with the increasing absolute value of V_g. This is because, although the channel is cut off due to the application of a gate negative voltage exceeding the threshold voltage, transient currents are generated due to the transient phenomena associated with the rising edge of the pulse voltage of V_g, which increase with the increment of V_g. On the other hand, when V_d is applied at 5 V, I_d' increases with the decreasing absolute value of V_g, reflecting the tendency for not only the transient component of the drain current but also the steady-state current to increase.

Figure 4(c) illustrates the correlation between I_d' and ΔT derived from Eq. (4) at each measurement point. It is evident that, at all measurement points, there is a positive correlation between I_d' and ΔT. This indicates that both the steady-state and transient components of the drain current, which constitute I_d', contribute to the temperature rise during device operation. Additionally, there is a trend of increasing ΔT values with respect to I_d' as the measurement point approaches the drain-side edge. We observe negative values of ΔT for several points in Fig. 4(c), which is possibly attributed to overestimation of piezoelectric strain component ($d'_{33}E_z$) in eq. (4), but it doesn't affect overall trends in the ΔT- I_d' relation. This also implies that the error in temperature measurement in this experiment is approximately 10 K. (We estimate that 20 percent errors (overestimation) in simulated electric field strength and inverse-piezo electric strain account for about 8 K difference (reduction) in the temperature estimation based on eq.(4)) The degree of the temperature rise at each measurement point is determined by the location of the heat source, assuming uniform heat dissipation characteristics near the channel. It is well-established from numerous previous studies that the drain-side gate electrode edge is a source of Joule heating due to electric field concentration, which validates this observation.

Directly comparing the ΔT values obtained in the present experiment with those obtained in previous studies using methods such as micro-Raman[23,26-28] is difficult, since the size of the present devices, the conditions of voltage application and the detected current components are different from those previously reported. Nevertheless, the fact that ΔT values of several K to several tens of K observed in this study is about an order

to half an order of magnitude smaller than previously reported results can be attributed to the larger device size and smaller current and voltage values used. For example, a previous paper reported that AlGaN/GaN HEMT on sapphire substrate shows temperature rise of about 200 K at 5 W/mm power condition.[33] This corresponds to temperature rise of about 10 K at 250 mW/mm, this is comparable to our present experimental condition. On the other hand, the successful detection of a temperature rise of only a few K clearly demonstrates that in-situ nanoXRD possesses sufficient capability to detect this level of temperature rise as a change in strain. The nanoXRD method is unique in that it can observe both lattice structure and temperature changes, which is advantageous in discussing the defect formation mechanism under nitride transistor operation. Furthermore, given that many inorganic semiconductor materials have a thermal expansion coefficient on the order of 10^{-6} K^{-1}, it can be asserted that in-situ nanoXRD, as demonstrated under the device operating conditions in this study, can also be applied to measure local temperature rises during the operation of devices in other material systems.

IV. CONCLUSION

We observed local lattice strain in the AlGaN/GaN MOS-HEMT by using in-situ nanoXRD pump-probe method. Position-dependent strain in the AlGaN barrier layer within the gate region was quantitatively measured under device operation with applied gate and drain voltages. In the *c*-axis strain, a position-dependent increase in strain values was observed as approaching from the center of the gate electrode to the drain-side gate electrode edge. Among the strains predominantly observed due to the inverse piezoelectric effect, the occurrence of thermal expansion strain was proposed as a particularly non-negligible strain component. This was substantiated by the time dependence of the transient and steady-state drain currents measured simultaneously with the strain measurements. To the best of our knowledge, this study is the first to derive temperature rise in an AlGaN/GaN HEMT device during operation by detecting thermal expansion strain using nanoXRD. Many causes of harmful defects in devices are often attributable to strain. Therefore, the findings of this study are significant as they demonstrate that not only the inverse piezoelectric effect but also the temperature rise of the device can be captured from the perspective of structural changes in the device.

Supplementary Material

Additional information about the FEM simulation of inverse-piezoelectric strain in AlGaN/GaN HEMT device is included in the supplementary material.

ACKNOWLEDGMENTS

The nanoXRD measurements were performed at the BL13XU beamline at SPring-8 with the approval of JASRI (Proposal Nos. 2019A1549, 2019B1009, 2019B1627, 2019B1797, 2019B2101, 2020A1136, 2020A1331, 2020A1402, 2020A1652, 2021A1207, 2021A1584, 2021B1345, 2021B1650, 2022B1567, 2022B1817, 2023A1695, 2023B1688, 2023B1052, 2024A1821, 2024A1929 and 2024B1651). This work was supported in part by JSPS KAKENHI (Grant Nos. JP16H06423, JP16H06421, JP22KK0055, and JP23H01447, JP23H05457) and Murata Science and Education Foundation.

DATA AVAILABILITY

The data that support the findings of this study are available from the corresponding author upon reasonable request.

REFERENCES

[1] N. Kaminski and O. Hilt, IET Circuits Devices Syst. **8**, 227–236 (2014). https://doi.org/10.1049/iet-cds.2013.0223

[2] K. Husna Hamza and D. Nirmal, Int. J. Electron. Commun. (AEÜ) **116**, 153040 (2020). https://doi.org/10.1016/j.aeue.2019.153040

[3] R. Sun, J. Lai, W. Chen, and B. Zhang, IEEE Access **8**, 15529–15542 (2020). https://doi.org/10.1109/ACCESS.2020.2967027

[4] O. Ambacher, B. Foutz, J. Smart, J. R. Shealy, N. G. Weimann, K. Chu, M. Murphy, A. J. Sierakowski, W. J. Schaff, and L. F. Eastman, J. Appl. Phys. **87**, 334–344 (2000). https://doi.org/10.1063/1.371866

[5] U. Chowdhury, J. L. Jimenez, C. Lee, E. Beam, P. Saunier, T. Balistreri, S.-Y. Park, T. Lee, J. Wang, M. J. Kim, J. Joh, and J. A. del Alamo, IEEE Electron Device Lett. **29**, 1098–1100 (2008). https://doi.org/10.1109/LED.2008.2003073

[6] S.Y. Park, C. Floresca, U. Chowdhury, J. L. Jimenez, C. Lee, E. Beam, P. Saunier, T. Balistreri, and M. J. Kim, Microelectronics Reliability **49**, 478–483 (2009). https://doi.org/10.1016/j.microrel.2009.02.015

[7] M. Tapajna, U. K. Mishra, and M. Kuball, Appl, Phys. Lett. **97**, 023503 (2010). https://doi.org/10.1063/1.3460529

[8] P. Makaram, J. Joh, J. A. del alamo, T. Palacios and C. V. Thompson, Appl. Phys. Lett. **96**, 233509 (2010). https://doi.org/10.1063/1.3446869

[9] M. Tapajna, N. Killat, J. Moereke, T. Paskova, K. R. Evans, J. Leach, X. Li, Ü. Özgür, H. Morkoç, and K. D. Chabak, IEEE Electron Device Lett. **33**, 1126–1128 (2012). https://doi.org/10.1109/LED.2012.2199278

[10] C-H. Lin, T. A. Merz, D. R. Doutt, J. Joh, J. A. del Alamo, U. K.Mishra, and L. J. Brillson, IEEE Trans. Electron Devices **59**, 2667–2674 (2012). https://doi.org/10.1109/TED.2012.2206595

[11] E. Zanoni, M. Meneghini, A. Chini, D. Macron, and G. Meneghesso, IEEE Trans. Electron Devices **60**, 3119–3131 (2013). https://doi.org/10.1109/TED.2013.2271954

[12] Y. Wu, C.-Y. Chen, and J. A. del Alamo, J. Appl. Phys. **117**, 025707 (2015). https://doi.org/10.1063/1.4905677

[13] A. Debnath, N. DasGupta, and A. DasGupta, IEEE Trans. Devices **67**, 834–840 (2020). https://doi.org/10.1109/TED.2020.2965561

[14] B. Shankar, A. Soni, S. Raghavan, and Mayank Shrivastava, IEEE Trans. Dev. Mater. Rel. 20, 767–774 (2020). https://doi.org/10.1109/TDMR.2020.3033522

[15] X. Cai, C. Du, Z. Sun, R. Ye, H. Liu, Y. Zhang, X. Duan, and H. Lu, J. Semicond. **42**, 051801 (2021). https://doi.org/10.1088/1674-4926/42/5/051801

[16] S. Kamada, S. Takeuchi, D. T. Khan, H. Miyake, K. Hiramatsu, Y. Imai, S. Kimura, and A. Sakai, Appl. Phys. Express **9**, 111001 (2016). https://doi.org/10.7567/APEX.9.111001
[17] Y. Ehara, S. Yasui, T. Oikawa, T. Shiraishi, T. Shimizu, H. Tanaka, N. Kanenko, R. Maran, T. Yamada, Y. Imai, O. Sakata, N. Valanoor, and H. Funakubo, Sci. Rep. 7, 9641 (2017). https://doi.org/10.1038/s41598-017-09389-6
[18] T. Sato, D, Ichinose, N. Oshima, T. Mimura, Y. Nemoto, T. Shimizu, Y. Imai, H. Uchida, O. Sakata, and H. Funakubo, Jpn. J. Appl. Phys. 57, 0902B8 (2018). https://doi.org/10.7567/JJAP.57.0902B8
[19] H. Shiomi, A. Ueda, T. Tohei, Y. Imai, T. Hamachi, K. Sumitani, S. Kimura, Y. Ando, T. Hashizume, and A. Sakai, Appl. Phys. Express **14**, 095502 (2021). https://doi.org/10.35848/1882-0786/ac1ee4
[20] T. Hamachi, T. Tohei, Y. Hayashi, S. Usami, M. Imanishi, Y. Mori, K. Sumitani, Y. Imai, S. Kimura, and A. Sakai, J. Appl. Phys. **135**, 225702 (2024). https://doi.org/10.1063/5.0199961
[21] Y. Ando, S. Kaneki, and T. Hashizume, Appl. Phys. Express **12**, 024002 (2019). https://doi.org/10.7567/1882-0786/aafded
[22] T. Hashizume, S. Kaneki, T. Oyobiki, Y. Ando, S. Sasaki, and K. Nishiguchi, Appl. Phys. Express **11**, 124102 (2018). https://doi.org/10.7567/APEX.11.124102
[23] S. Choi, E. R. Heller, D. Dorsey, R. Vetury, and S. Graham, IEEE Trans. Electron Devices **60**, 159–162 (2013). https://doi.org/10.1109/TED.2012.2224115
[24] B. M. Paine, T. Rust, and E. A. Moore, IEEE Trans. Electron Devices **63**, 590–597 (2016). https://doi.org/10.1109/TED.2015.2510610
[25] X. Chen, S. Boumaiza, and L. Wei, IEEE Trans. Electron Devices **66**, 3748–3755 (2019). https://doi.org/DOI: 10.1109/TED.2019.2926742
[26] A. Sarua, H. Ji, M. Kuball, M. J. Uren, T. Martin, K.P. Hilton, and R. S. Balmer, IEEE Trans. Electron Devices **53**, 2438–2447 (2006). https://doi.org/10.1109/TED.2006.882274
[27] K. R. Bagnall, E. A. Moore, S. C. Badescu, L. Zhang, and E. N. Wang, Rev. Sci. Inst. **88**, 113111 (2017). https://doi.org/10.1063/1.5010225
[28] M. Wu, X.-H. Ma, L. Yang, Q. Zhu, M. Zhang, L.-A. Yang, and Y. Hao, IEEE Trans. Electron Devices, **65**, 4792–4799 (2018). https://doi.org/10.1109/TED.2018.2868807
[29] K. Lefki and G. J. M. Dormans, J. Appl. Phys. **76**, 1764–1767 (1994). https://doi.org/10.1063/1.357693
[30] I. L. Guy, S. Muensit, and E. M. Goldys, Appl. Phys. Lett. **75**, 4133–4135 (1999). https://doi.org/10.1063/1.125560

[31] I. Vurgaftman and J. R. Meyer, J. Appl. Phys. **94**, 3675–3696 (2003).
https://doi.org/10.1063/1.1600519
[32] R. R. Reeber and K. Wang, MRS Online Proceedings Library **622**, 6351 (2000).
https://doi.org/10.1557/PROC-622-T6.35.1
[33] S. Martin-Horcajo, A. Wang, M-F. Romero, M. J. Tadjer, F. Calle, IEEE Trans. El. Dev. **60**, 4105 (2013).
https://doi.org/10.1109/TED.2013.2284851

Figures

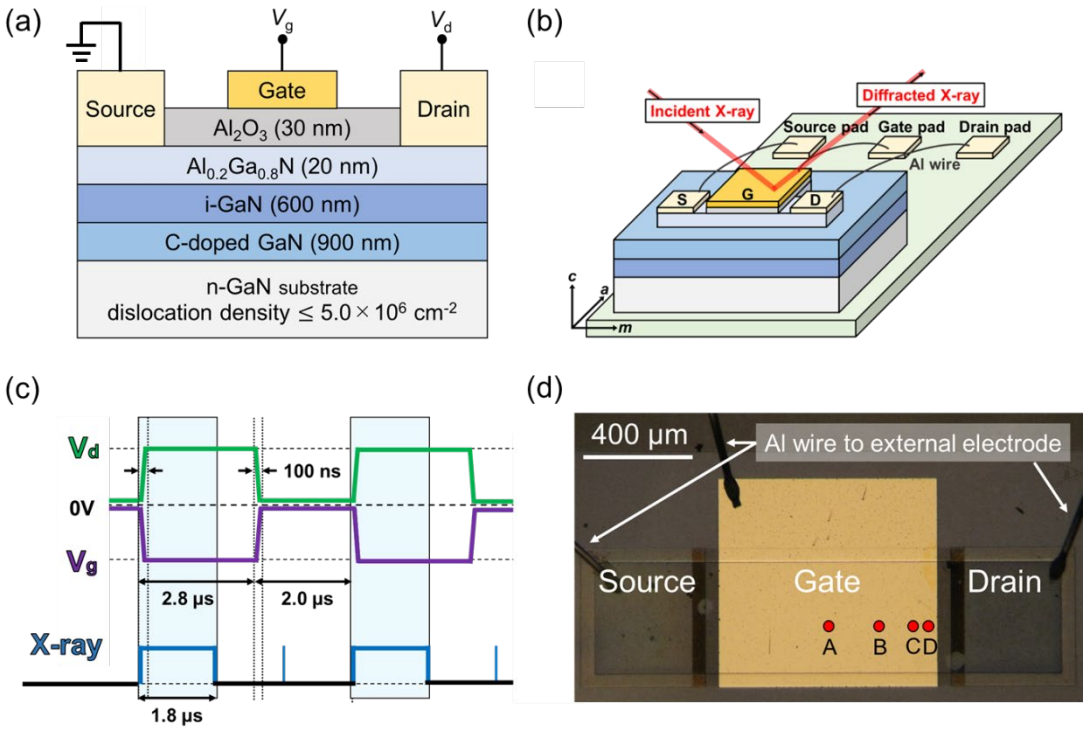

FIG. 1. (a) Schematic cross section of the AlGaN/GaN MOS-HEMT structure, (b) Schematic of the X-ray diffraction geometry in which each electrode is equipotential with Al wire, (c) The voltage application and X-ray irradiation protocol: V_d = 0 V and 5 V pulse, and (d) The X-ray irradiation points: 400, 200, 50, and 10 μm apart from the drain side gate edge (points A, B, C, and D).

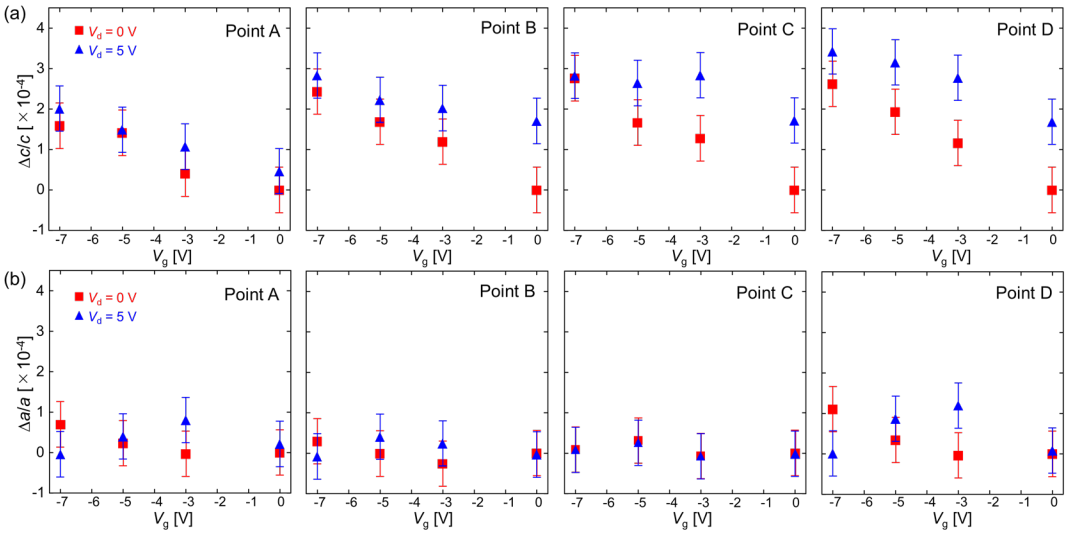

FIG. 2. Measured strains in (a) the *c*-axis ($\Delta c/c$) and (b) the *a*-axis ($\Delta a/a$) of the AlGaN layer as a function of applied gate voltage V_g with different drain voltages V_d for points A to D.

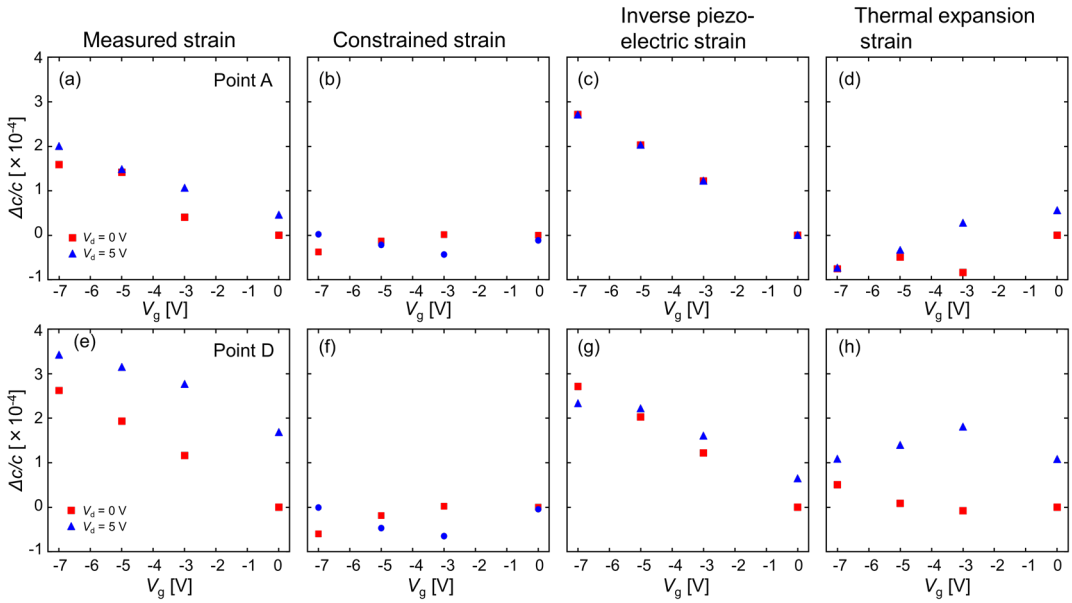

FIG. 3. Results of decomposing the measured strains at (a-d) point A and (e-h) point D into the components of constrained strain (b,f), inverse piezoelectric strain (c,g), and thermal expansion strain(d,h), based on Eq. (3).

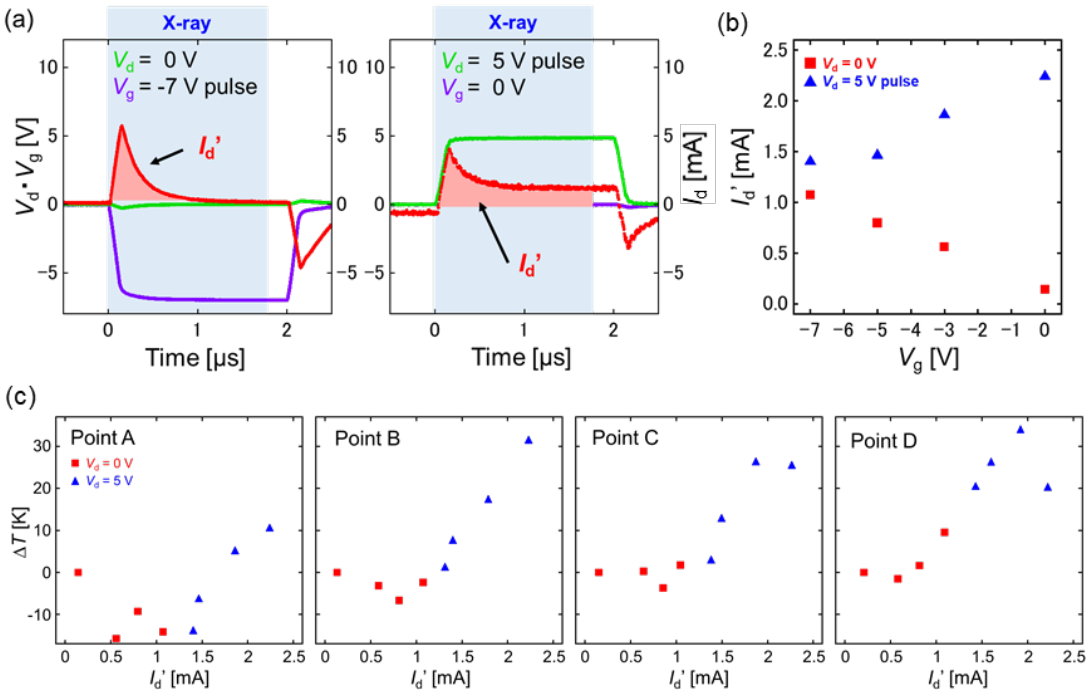

FIG. 4. (a) Voltage and current characteristics of the device as a function of time during nanoXRD measurements under two different voltage application condition. The green, purple, and red lines represent the drain voltage, the gate voltage, and the drain current, respectively. The duration of X-ray irradiation is shaded in light blue. (b) Drain current I_d' as a function of V_g for different V_d measured at point A. (c) Relationship between I_d' and the temperature rise ΔT at measurement points A to D (red and blue symbols show V_d= 0 and 5 V conditions, respectively).